Article

Synthesis and Characterization of Novel Nanoparticles of Lithium Aluminum Iodate LiAl(IO$_3$)$_4$, and DFT Calculations of the Crystal Structure and Physical Properties

Rihab Chikhaoui [1], Zoulikha Hebboul [1], Mohamed Abdelilah Fadla [2], Kevin Bredillet [3], Akun Liang [4], Daniel Errandonea [4], Sandrine Beauquis [3], Ali Benghia [2], Jean Christophe Marty [3], Ronan Le Dantec [3], Yannick Mugnier [3] and Enrico Bandiello [4,*]

[1] Laboratoire Physico-Chimie des Matériaux (LPCM), Université Amar Telidji de Laghouat, BP 37G, Laghouat 03000, Algeria; rihabchikhaoui.26@gmail.com (R.C.); z.hebboul@lagh-univ.dz (Z.H.)
[2] Laboratoire de Physique des Matériaux, Université Amar Telidji de Laghouat, BP 37G, Laghouat 03000, Algeria; ma.fadla@lagh-univ.dz (M.A.F.); benghia11@gmail.com (A.B.)
[3] SYstème et Matériaux pour la MÉcatronique (SYMME), University Savoie Mont Blanc, F-74000 Annecy, France; kevin.bredillet@univ-smb.fr (K.B.); Sandrine.Beauquis@univ-smb.fr (S.B.); Jean-Christophe.Marty@univ-savoie.fr (J.C.M.); Ronan.le-Dantec@univ-smb.fr (R.L.D.); Yannick.Mugnier@univ-smb.fr (Y.M.)
[4] Departamento de Física Aplicada—ICMUV—MALTA Consolider Team, Universitat de València, c/Dr. Moliner 50, 46100 Burjassot, València, Spain; akun2.liang@uv.es (A.L.); Daniel.Errandonea@uv.es (D.E.)
* Correspondence: enrico.bandiello@uv.es

Abstract: Here we report on the non-hydrothermal aqueous synthesis and characterization of nanocrystalline lithium aluminum iodate, LiAl(IO$_3$)$_4$. Morphological and compositional analyses were carried out by using scanning electron microscopy (SEM) and energy-dispersive X-ray measurements (EDX). The optical and vibrational properties of LiAl(IO$_3$)$_4$ have been studied by UV-Vis and IR spectroscopy. LiAl(IO$_3$)$_4$ is found to crystallize in the non-centrosymmetric, monoclinic $P2_1$ space group, contrary to what was reported previously. Theoretical simulations and Rietveld refinements of crystal structure support this finding, together with the relatively high Second Harmonic Generation (SGH) response that was observed. Electronic band structure calculations show that LiAl(IO$_3$)$_4$ crystal has an indirect band gap $E_{\text{gap}} = 3.68$ eV, in agreement with the experimental optical band gap $E_{\text{gap}} = 3.43(3)$ eV. The complex relative permittivity and the refraction index of LiAl(IO$_3$)$_4$ have also been calculated as a function of energy, as well as its elastic constants and mechanical parameters. LiAl(IO$_3$)$_4$ is found to be a very compressible and ductile material. Our findings imply that LiAl(IO$_3$)$_4$ is a promising material for optoelectronic and non-linear optical applications.

Keywords: precipitation; crystal structure; X-ray diffraction; scanning electron microscopy; optical spectroscopies; computer simulations

1. Introduction

Inorganic nanoparticles usually exhibit interesting magnetic, electrical, and optical properties, including non-linear optical (NLO) features. Many methods for the synthesis of inorganic nanoparticles exist, encompassing physical, chemical, and mechanical processes. The choice of the synthesis method is dictated by the structure that has to be obtained which, in turn, depends on the foreseen applications [1,2]. In fact, the nanoparticle size and size-distribution, the surface area, the chemical composition, as well as the purity, shape, and surface structure of the nanoparticles, play key roles in the resulting functional properties. Broadly speaking, synthesis methods can be subdivided into two categories: constructive methods and destructive methods. The former consists of the build-up of materials from single atoms to clusters and to nanoparticles, by methods including sol-gel [3,4],

spinning [5], chemical vapor deposition [6], pyrolysis [7], and biosynthesis [8]. Conversely, in destructive methods, the reduction of bulk material to nanometric particles takes place through mechanical milling [9], nanolithography [10], laser ablation [11], sputtering [12], and thermal decomposition [13].

Non-centrosymmetric inorganic nanoparticles exhibit non-linear optical features (NLO), with generation of several harmonics and possible up-conversion of signals [14,15]. Nanocrystals have also been developed extensively for potential biomedical applications, molecular sensing devices, diagnostic imaging, and localization at tumor sites [16,17]. Many different families of nanomaterials have been studied with the aim of enhancing medical and NLO applications [18–20]. Metal iodates are considered to be among the most interesting nanomaterials [21–29], not only for NLO but also because of their dielectric properties and their unusual bonding properties, related to the presence of an electron lone pair on the iodine atom [30–38].

Hydrothermal and solvothermal synthesis methods are typically the most promising approaches for the preparation of metal iodate nanomaterials. These methods can be combined with microwave heating to improve the quality and the reproducibility of the final products [14].

In the first part of this work, we describe for the first time a simple and inexpensive chemical route for the preparation of pure nanocrystals of $LiAl(IO_3)_4$, which is a novel and interesting material for optoelectronics and nonlinear optics. $LiAl(IO_3)_4$ nanocrystals have been synthetized using a soft-chemistry method, which takes advantage of the direct precipitation reaction between lithium iodate ($LiIO_3$) and aluminum nitrate nonahydrate ($Al(NO_3)_3 \cdot 9H_2O$) from highly concentrated water solutions, without hydrothermal conditions. To the best of our knowledge, this is one of the first examples of such a simple chemical route for the preparation of iodate nanoparticles. The morphology of the final product was inspected by electron microscopy, and the average size of particles was measured by X-ray diffraction, using Le Bail fir refinement and the Williamson-Hall method (W-H). UV-Vis and infrared spectra were also measured and discussed. Preliminary results dealing with a crude estimation of the SHG efficiency of $LiAl(IO_3)_4$ were also included after comparison of the emitted signals from two colloidal suspensions, the reference sample being $LiNbO_3$ nanocrystals of similar size. The optical band gap of $LiAl(IO_3)_4$ nanoparticles was measured experimentally by absorbance spectroscopy. The second part of the manuscript is devoted to the theoretical calculation of the structural model and physical properties of this new compound using the Density-Functional Theory (DFT).

2. Materials and Methods

2.1. Sample Preparation and Characterization

Reagents purchased from Sigma–Aldrich (Burlington, MA, USA), lithium iodate ($LiIO_3$, 99.5%) and aluminum nitrate nonahydrate ($Al(NO_3)_3 \cdot 9H_2O$, 98%), were used without further purification. Powder X-ray diffraction patterns (XRD) of the final product were obtained at ambient conditions using a Panalytical EMPYREAN MALVERN (Malvern, UK) powder diffractometer (Cu Kα_1, 40 mA, 30 kV) with a 0.01° step size and an acquisition time of 6 s/step in the 17–85° 2θ range. The homogeneity and chemical composition of the sample were investigated by Scanning Electron Microscopy (SEM) using a Tescan Vega (Brno - Kohoutovice, Czech Republic) electron microscope system attached to a Peltier-cooled XFlashTM (Bruker AXS—Karlsruhe, Germany) silicon drift detector, model 410 M, for energy dispersive X-ray (EDX) analysis. Optical absorption spectra were recorded using a Jasco V-630 UV-Vis (Easton, MD, USA) spectrophotometer in the 190–1100 nm wavelength range. Infrared spectra (FTIR) were recorded on a Jasco FT/IR-4200 (Easton, MD, USA) setup between 1000 and 400 cm^{-1} using KBr pellets. Dynamic light scattering (DLS) measurements (Zetasizer Nano, Malvern Panalytical, Palaiseau, France) were used to assess the colloidal stability and aggregation state of the synthesized samples after re-dispersion in ethanol.

2.2. Ab-Initio Calculations

The performed ab-initio calculations were based on the DFT theory [39,40] to calculate the structural, electronic, mechanical, and linear optical properties, using the pseudopotential plane-wave (PP-PW) method as implemented in the Cambridge Sequential Total Energy Package (CASTEP) module of Material Studio [39]. The exchange correlation interaction was described by the generalized-gradient approximation (GGA), using the Perdew-Burke-Ernzerhof (PBE) parameterization [40], with a kinetic cut-off energy of 700 eV for the plane-wave expansions. The reciprocal space integration was performed using (6 10 6) k-point grids in the first Brillouin zone (BZ). The geometry optimization was performed using the Broyden–Fletcher–Golfard–Shannon (BFGS) algorithm. The ultra-soft pseudopotential was used within the following valence electronic configuration: Li: $1s^2 2s^1$; O: $2s^2 2p^4$; Al: $3p^1 4s^2$; and I: $5s^2 5p^5$. For band structure calculations, in addition to the PBE functional we have implemented the nonlocal hybrid functional HSE06 (Heyd–Scuseria–Ernzerhof) [41], for a more precise determination of gap energy.

3. Results and Discussion

3.1. Synthesis and XRD Characterization

A white precipitate of nanoparticles of pure $LiAl(IO_3)_4$ was collected, after a few hours, from an aqueous solution of 4 mmol $LiIO_3$ and 1 mmol of $Al(NO_3)_3 \cdot 9H_2O$, dissolved in 3 mL of distilled water. The volume of water was kept to the minimum that allowed for the dissolution of the reagents, i.e., the solution was almost saturated. The reaction mixture was subsequently dried in an oven at 70 °C, until the water was completely evaporated. After drying, no residual reagents were found, implying a complete reaction. This was confirmed by EDX analysis (Figure 1), demonstrating the correct stoichiometry and the absence of residual reagents. Within the experimental error, EDX analyses of Al and I content by both weight percent and atomic percent agreed with the expected molar ratio of 1:4. Numerically, the measured Al and I contents were 19.97 at% and 80.03 at%, respectively. As no impurities were detected, the elementary analysis shown in Figure 1 confirmed the composition of the as-prepared $LiAl(IO_3)_4$ samples. The morphology of the synthetized material is shown in the SEM image of Figure 2, exhibiting nano-powder agglomerates with cotton flower shapes.
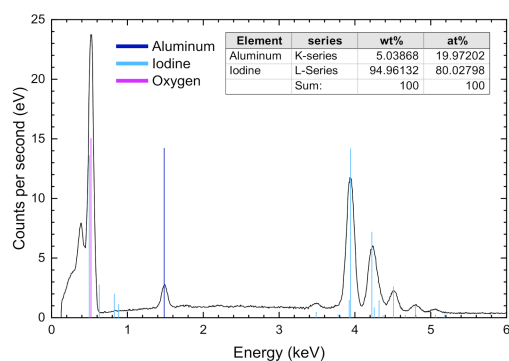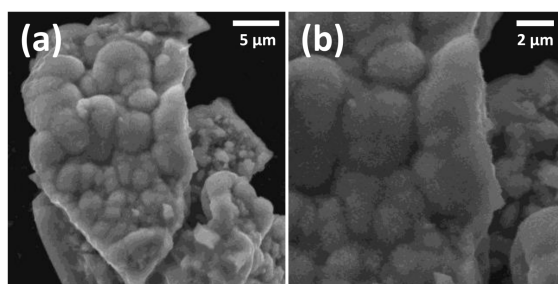

Element	series	wt%	at%
Aluminum	K-series	5.03868	19.97202
Iodine	L-Series	94.96132	80.02798
	Sum:	100	100

**Figure 1.** EDX elementary analysis of $LiAl(IO_3)_4$. No traces of impurities were found in our sample.

Figure 2. SEM image showing morphology of the nanopowders of LiAl(IO₃)₄ at two different magnifications. White bars in the figures indicate the scale, respectively (**a**) 5 μm, and (**b**) 2 μm.

Figure 3 shows the X-ray diffraction patterns of LiAl(IO$_3$)$_4$ nanoparticles. To the best of our knowledge, the only mention of LiAl(IO$_3$)$_4$ in the literature is in Ref. [42]. A hexagonal structure (space group $P6_3$) was proposed, with lattice constants $a = 5.585$ Å and $c = 4.945$ Å. This structure was derived from the structure of LiIO$_3$, assuming that Li and Al atoms in LiAl(IO$_3$)$_4$ randomly occupy the atomic positions of Li in LiIO$_3$ with a 0.5 occupancy factor. However, this structure does not satisfy the stoichiometry of the compound and does not result in the density measured previously [42] and in this work. In addition, we found that a structure based on the $P6_3$ space group cannot properly index all the experimental XRD peaks, as demonstrated by the green ticks in Figure 3 for a hexagonal indexation. In fact, an indexation with the hexagonal structure led to $a = 10.649$ Å and $c = 5.182$ Å for the unit-cell parameter, with a being almost twice the value previously reported [42]. This suggests that the structure previously reported is not correct and that a lower symmetry structure is needed to account for all experimental diffraction peaks. We found that a monoclinic structure isomorphic to Co(IO$_3$)$_2$ (space group $P2_1$) can satisfactorily explain the XRD pattern measured for LiAl(IO$_3$)$_4$ [43]. This can be seen in Figure 3, where we show the result of a Rietveld refinement and the calculated positions of the different (hkl) reflections. Because of the small nanoparticle size and the significant FWHM of the XRD peaks, a full structural refinement is not yet allowed. Instead, we built a crystal structure based on Co(IO$_3$)$_2$, assuming two independent positions for Co atoms: one occupied by Li atoms and the other by Al atoms. This structure was subsequently optimized by means of tn Table 1.
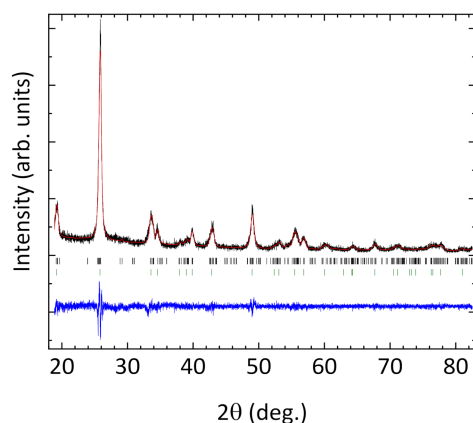

Figure 3. XRD pattern and Rietveld refinement of LiAl(IO$_3$)$_4$ nanopowders. Black line: experimental data; red line: Rietveld refinement; blue line: residuals; black and green ticks: Bragg reflections calculated using the monoclinic $P2_1$ and the hexagonal $P6_3$ space group, respectively. R-factors of the Rietveld refinement: $R_p = 10.41\%$, $R_{wp} = 14.28\%$, $\chi^2 = 1.29$.

Table 1. Atomic positions of LiAl(IO$_3$)$_4$.

Atom	Wyckoff Position	Atomic Position		
		x/a	y/b	z/c
Al	2a	0.495	0.2942	0.2394
Li	2a	0.0062	0.7938	0.2617
I$_1$	2a	0.1832	0.2101	0.5818
I$_2$	2a	0.6846	0.2107	0.0857
I$_3$	2a	0.154	0.2251	0.087
I$_4$	2a	0.6525	0.2241	0.5838
O$_1$	2a	0.319	0.023	0.72
O$_2$	2a	0.158	0	0.441
O$_3$	2a	0.038	0.093	0.5989
O$_4$	2a	0.547	0.072	0.115
O$_5$	2a	0.833	0.046	0.228
O$_6$	2a	0.342	0.528	0.072
O$_7$	2a	0.312	0.067	0.185
O$_8$	2a	0.109	0.059	0.922
O$_9$	2a	0.0333	0.031	0.1193
O$_{10}$	2a	0.452	0.487	0.376
O$_{11}$	2a	0.176	0.562	0.295
O$_{12}$	2a	0.616	0.085	0.4146

The atomic positions obtained from DFT were assumed for the Rietveld refinement. They were fixed during the refinement; only the unit-cell parameters, background, and peak-shape parameters were used as fitting parameters. We obtained $a = 10.579(4)$ Å, $b = 5.183(2)$ Å, $c = 10.701(4)$ Å, and $\beta = 119.88(5)°$. The goodness of the fit refinement parameters were $R_\mathrm{p} = 10.41\%$, $R_\mathrm{wp} = 14.28\%$, and $\chi^2 = 1.29$. As illustrated in Figure 4, the Li^{1+} and Al^{3+} cations are coordinated to six O atoms and form slightly distorted octahedral units, which are connected by IO$_3$ triangular pyramids. This coordination for I^{5+} ions is typical of metal iodates, being related to the existence of a lone pair of electrons of the I atom in the IO$_3$ molecule. In the proposed crystal structure, each octahedral unit is surrounded by six IO$_3$ groups. Regarding the nanoparticle size leading to the XRD peak-broadening, the Le Bail global fitting procedure was implemented by assuming a spherical morphology and the absence of any strain, and by considering the Lorentzian and Gaussian parts of the peak shape. The nanocrystal size thus derived at 22.7 nm is in good agreement with the value at ≈22.9 nm obtained by the Williamson-Hall method [44–46].
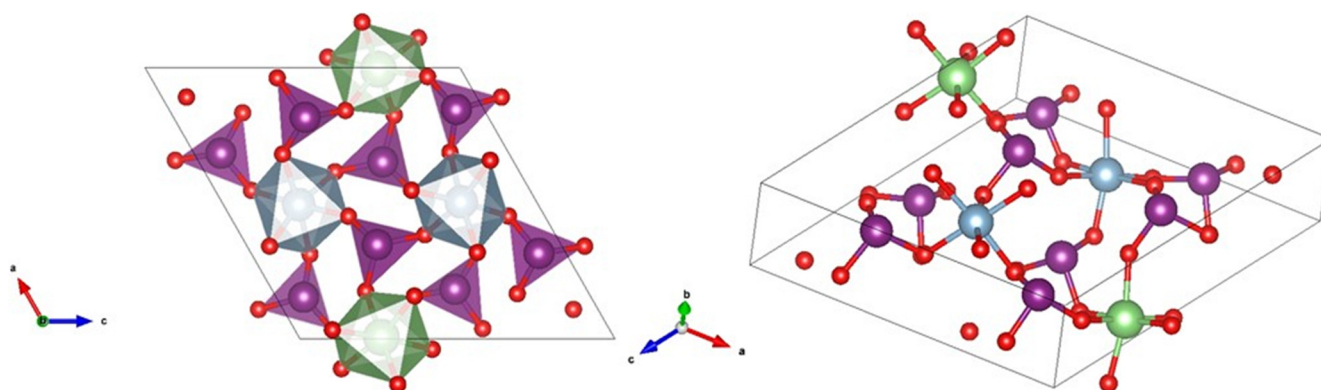

Figure 4. Schematic representation of the crystal structure of LiAl(IO$_3$)$_4$ from different views. The AlO$_6$ and LiO$_6$ octahedra are shown (in cyan and green, respectively) as well as the IO$_3$ triangular pyramids (in violet).

3.2. FTIR, UV-Vis and SHG Measurements

The results of Fourier-transform infrared spectroscopy (FTIR) measurements are discussed in the following. Figure 5a shows the IR transmission spectrum in the 1000–400 cm^{-1}

range. By analogy with other iodates, the two vibrational frequencies of LiAl(IO$_3$)$_4$ observed at around 660 cm^{-1} and 786 cm^{-1} can be tentatively assigned as the symmetric (ν_1 at 780–630 cm^{-1}) and anti-symmetric (ν_3 at 730–820 cm^{-1}) stretching internal modes of the pyramidal IO$_3^-$ ion, respectively. These values are compatible with the equivalent modes of Al(IO$_3$)$_3$ [47], La(IO$_3$) [22], Zn(IO$_3$)$_2$ [26], and LiZn(IO$_3$)$_3$ [37], among other iodates.
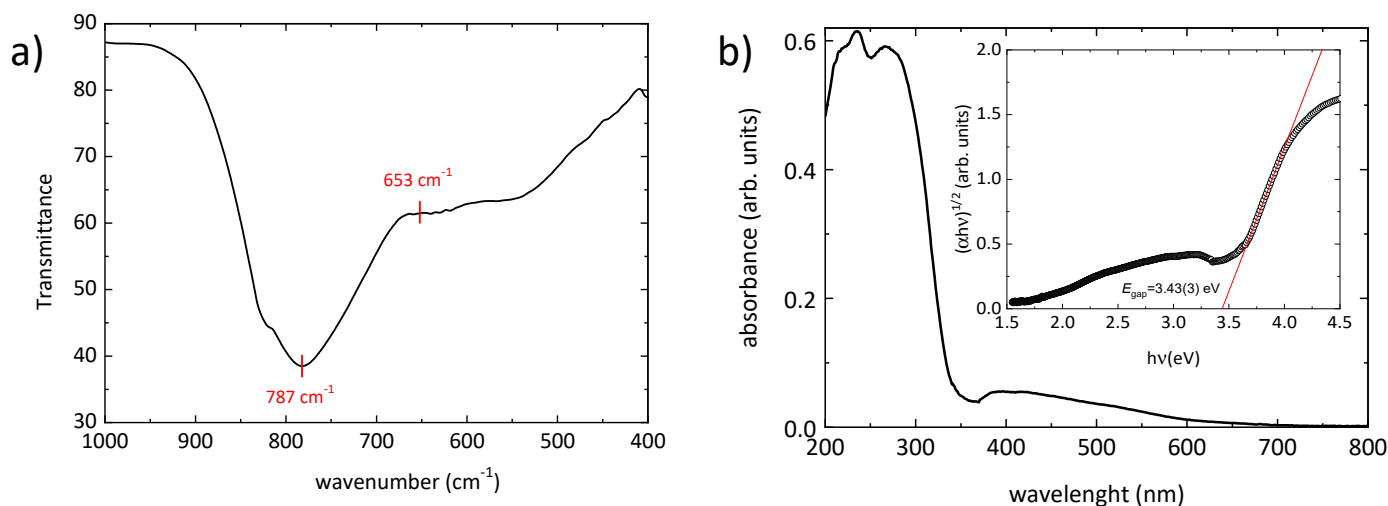
Figure 5. (**a**) FTIR transmission spectrum of nanocrystalline LiAl(IO$_3$)$_4$ in the 1000–400 cm^{-1} range; (**b**) UV-Vis absorption spectrum. The inset in (**b**) shows the determination of the band gap E_{gap} by means of a Tauc plot of the absorbance of LiAl(IO$_3$)$_4$ (indirect band gap).

As shown in the following discussion, according to our DFT calculations, the band gap of LiAl(IO$_3$)$_4$ is indirect. Thus, the value E_{gap} = 3.43(3) eV of the band gap wass estimated by extrapolating the linear part of the $(\alpha h\nu)^{1/2}$ curve as a function of the incident phonon energy $h\nu$ (α being the absorbance) in a Tauc plot (Figure 5b) [48].

The optical properties of the particles were explored using UV-Vis absorption spectroscopy. The absorption spectrum of LiAl(IO$_3$)$_4$ nanoparticles, as shown in Figure 5b, exhibits strong absorbance below 250 nm. An excitonic absorption peak is found at about 275 nm (eV), with an exciton binding energy E_B = 1.08 eV.

Finally, because of the non-centrosymmetric space group $P2_1$ derived above, SHG properties were expected for LiAl(IO$_3$)$_4$. To get a rapid insight of its SHG efficiency, a suspension was initially prepared at 1 g/L, after sonication of the raw powder in ethanol. After sedimentation for 10 h, drying and weighing of the larger aggregates that had settled down allowed an estimation of the final mass concentration at 0.7 g/L within the supernatant. The corresponding DLS size distribution in intensity is indicated in the inset of Figure 6. The mean size centered at ~255 nm, together with a relatively high PDI value at 0.22, indicated the presence of remaining aggregates whose hydrodynamic diameters were significantly larger than the 23 nm XRD crystallite size derived above. For comparison, a colloidal suspension of LiNbO$_3$ nanocrystals, of mean DLS at 120 nm and small PDI value at 0.09, was also prepared at 1 g/L in ethanol. The corresponding mean XRD size at ~30 nm and the synthesis method are described elsewhere [49]. Both suspensions containing LiNbO$_3$ and LiAl(IO$_3$)$_4$ nanocrystals of similar XRD mean size and mass concentration were prepared with the aim of obtaining a rapid comparison of their SHG conversion efficiencies from Second Harmonic (SH) spectroscopy, with the setup fully described in Ref. [50]. Here, for two excitation wavelengths arbitrarily fixed at 800 nm and 1064 nm, the scattered SH intensities are plotted in Figure 6 for the same experimental parameters in the excitation and detection arms. Interestingly, the SHG response of the LiAl(IO$_3$)$_4$ nanocrystal suspension was found to be above that of the reference LiNbO$_3$ material. At this stage, because of the partial aggregation state within the LiAl(IO$_3$)$_4$ nanocrystal suspension and the eventual presence of a broad size dispersion that would require further TEM imaging,

a quantitative assessment of the orientation-averaged second-order susceptibility was difficult to achieve, although promising NLO performances were clearly demonstrated for the iodate modification.
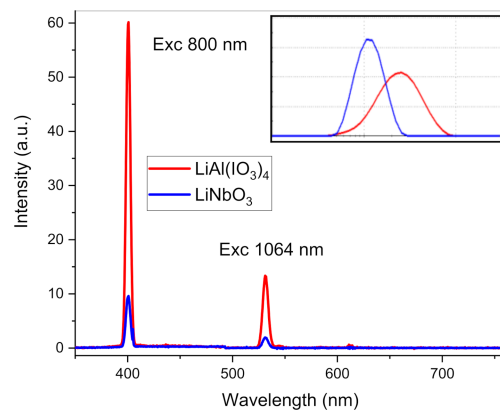
Figure 6. SH scattered intensities collected from a $LiAl(IO_3)_4$ (red curve) and a $LiNbO_3$ (blue curve) nanocrystal suspension with similar XRD crystallite sizes and mass concentrations for two excitation wavelengths fixed at 800 nm and 1064 nm. In the inset, the corresponding DLS size distributions in intensity are plotted, showing a higher aggregation state within the supernatant of the $LiAl(IO_3)_4$ suspension.

3.3. Ab-Initio Calculations

Ab initio simulations were used to calculate the crystal structure of $LiAl(IO_3)_4$. The structure was modeled starting from the isostructural $Co(IO_3)_2$, in which the two independent cobalt atoms were substituted by Li and Al. Subsequently, we performed the optimization of the equilibrium geometry, determining atomic coordinates and lattice parameters. Forces (stresses) on atoms (lattice) were minimized using the Hellmann-Feynman theorem [51,52]. The calculated lattice parameters were $a = 10.80(5)$ Å, $b = 5.14(4)$ Å, $c = 10.89(4)$ Å, and $\beta = 119.00(3)°$ ($V = 528.49(9)$ Å^3), which agreed within 1% with those we obtained from the refinements. The calculated atomic positions are summarized in Table 1. The molar mass of $LiAl(IO_3)_4$ was found to be 1467.07 g mol^{-1}, and it has two formula units per cell ($Z = 2$), with a density of $\rho = 4.61$ g cm^{-3}. From these calculations, we obtained information on the bond distances. The polyhedron corresponding to the iodate groups $IO_3{}^-$ exhibited the expected trigonal-pyramidal symmetry, with four different iodine atoms. As can be seen in Table 2, each iodine atom is connected to three oxygen atoms by short bonds.

Table 2. Interatomic bond distances d in the coordination polyhedra of $LiAl(IO_3)_4$.

Atom 1	Atom 2	d (Å)	Atom 1	Atom 2	d (Å)	Atom 1	Atom 2	d (Å)
	O_{10}	2.020		O_{11}	2.066		O_3	1.772
	O_{12}	2.021		O_3	2.073	I_1	O_2	1.785
Al	O_4	2.047	Li	O_9	2.101		O_1	1.789
	O_7	2.118		O_2	2.126			
	O_6	2.139		O_8	2.143			
	O_1	2.180		O_5	2.156			
	O_5	1.810		O_7	1.716		O_{12}	1.832
I_2	O_4	1.811	I_3	O_9	1.806	I_4	O_{10}	1.852
	O_6	1.853		O_8	1.829		O_{11}	1.870

The LiO_6 octahedral units are slightly distorted. The Li^+ cation is connected by three monodentate bonds with an average I–O length of 2.08 Å and with three additional iodate groups with an average I–O length of 2.14 Å (Figure 4). Similarly, AlO_6 units are also slightly distorted octahedral units connected to IO_3 pyramids in a similar way to LiO_6.

From DFT calculations, we also determined the electronic band structure of $LiAl(IO_3)_4$, as shown in Figure 7. We found that the material is an indirect semiconductor, with the top of the valence band at the Z point of the Brillouin zone and the bottom of the conduction band between B and D. The calculated band gap was $E_{gap} = 2.43(9)$ eV or $E_{gap} = 3.68$ eV, as calculated by the GGA (PBE) or the HSE06 approach, respectively. The first value underestimated the band gap, a known fact fore PBE functionals, while the hybrid HSE06 functional provided excellent agreement with the calculations. While the band dispersion is well described by PBE, this functional as well as other widely used local functionals, fails in computing the gap value. Therefore, the scissor operator (i.e., the difference between the theoretical value and the most reliable band gap values) was used in this case, which finally gave the same value for the band gap as for HSE06: $E_{gap} = 3.68$ eV.
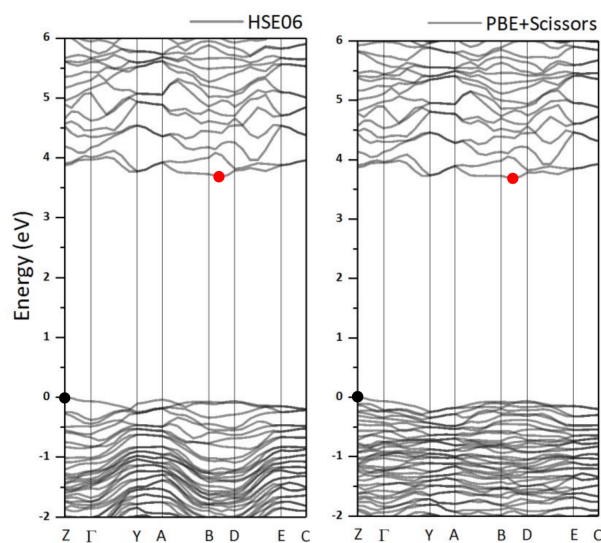
Figure 7. Band structure of $LiAl(IO_3)_4$, as calculated by HDE06 (**left**) and PBE with the scissor parameter (**right**). The red and the black dots represent the top of the valence band and the bottom of the conduction band, respectively.

The projected density of the states of $LiAl(IO_3)_4$ (PDOS) is shown in Figure 8. The valence band of $LiAl(IO_3)_4$ can be divided into two regions with respect to energy. The first region is in the range of -20 to -10 eV, where the bands are attributed to the I s states mixed with some O s states, corresponding to a short, strong covalent I–O bond. Contributions of the s and p orbitals of Al are weak in the second energy region, from -7 to 0 eV, since it is dominated instead by the p orbitals of I and O, with the latter being the main contribution to the top of the valence band. The bottom of the conduction band, in the range of 0 to 10 eV, is mainly dominated by the p orbitals of the iodine atom, with a negligible contribution of the s and p orbitals of the Al and O p states.

The features observed here, from the calculated PDOS of $LiAl(IO_3)_4$, are in a good agreement with those of other non-transition metal iodates widely reported in the literature [23,53–57]. Moreover, as we pointed out in our previous work, if there is no transition metal in the metal iodates, the valence band maxima (VBM) will mainly be dominated by the O 2p orbitals, and the conduction band minima (CBM) will mainly be dominated by the I 5p orbitals [57]. On the other hand, the partially filled d orbitals of transition metal will usually contribute to either the VBM or CBM, thus narrowing the band gap. Based on this fact, the non-transition metal iodates are usually expected to have a relatively large band gap, which can explain the large band gap found here in $LiAl(IO_3)_4$.
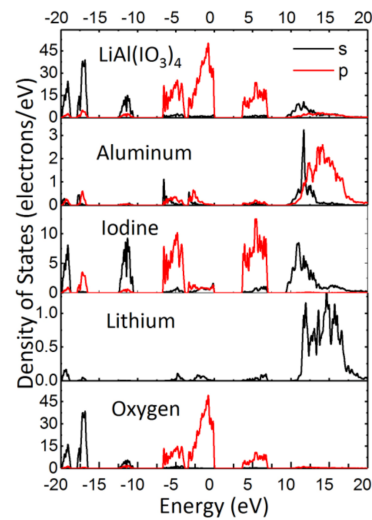
Figure 8. Calculated total distribution of states (DOS) of $LiAl(IO_3)_4$ (top), and partial DOS due to aluminum, iodine, and oxygen atoms in the $LiAl(IO_3)_4$ structure. Black lines: contribution of *s* states; red lines: contribution of *p* states. The calculations were performed using the PBE + scissor method.

We also studied the linear optical properties of $LiAl(IO_3)_4$, calculating the complex relative permittivity $\varepsilon(\omega) = \varepsilon_1(\omega) + i\varepsilon_2(\omega)$. The curves of the dielectric function of $LiAl(IO_3)_4$ as a function of the photon energy along the main crystallographic axes, [100], [010], and [001], are shown in Figure 9a. The scissor correction was also added in the computation of optical properties, to avoid underestimation of the band gap due to PBE.
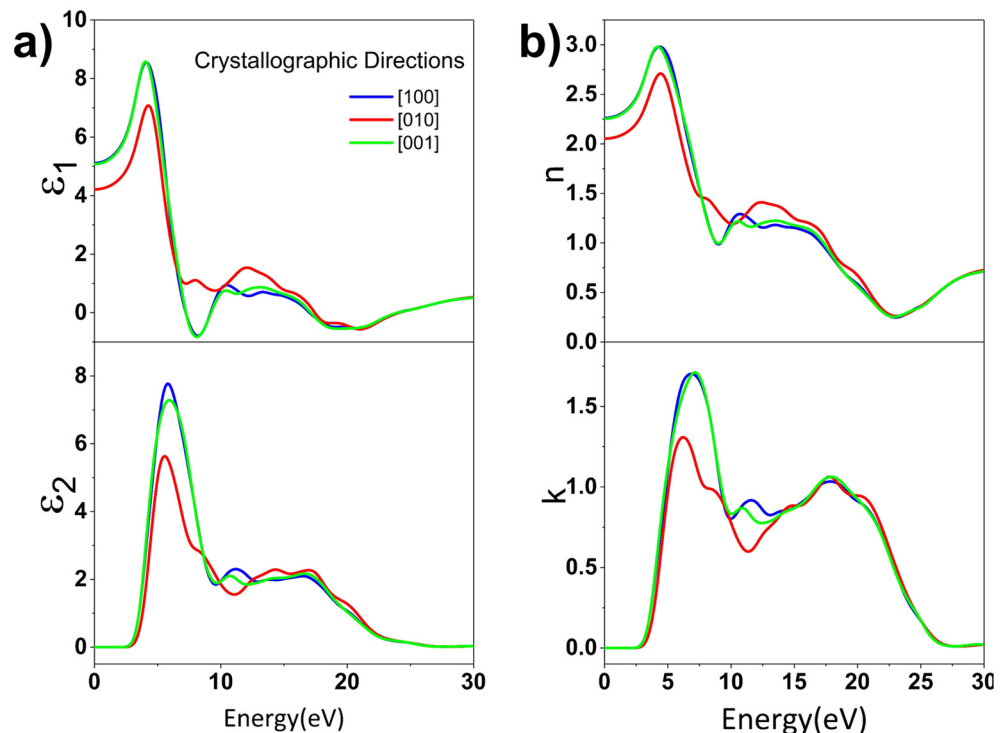
Figure 9. (**a**) Calculated real (ε_1) and imaginary (ε_2) parts of the dielectric function of $LiAl(IO_3)_4$ as a function of the incident photon energy and (**b**) corresponding real (*n*) and imaginary (*k*) parts of the refractive indexes. The line color is indicated for each crystallographic direction. These calculations have been performed with the PBE + scissor method.

The value of the $\varepsilon_1(0)$ static dielectric constant is about 5, on average. The dispersion curves of the complex refractive index $\underline{n} = n + ik$, along the main crystallographic

directions, are depicted in Figure 9b and show a strong anisotropy between the optical components that are parallel and perpendicular to the [010] direction, in the plane (010) and the direction perpendicular to it [010]. This implies that $LiAl(IO_3)_4$ is a birefringent material, one of the most desirable features for active NLO materials [58,59]. Based on the difference between the refractive indices n_{100} and n_{010} (2.47 (2.26) and 2.22 (2.05) without/with scissor, respectively), the birefringence index of $LiAl(IO_3)_4$, is $D_n = 0.21$. Note that zinc iodate ($Zn(IO_3)_2$) and lithium zinc iodate ($LiZn(IO_3)_3$), both crystallizing in the $P2_1$ space group, have similar birefringence indices at 0.33 and 0.29, respectively [23]. Incidentally, as $LiAl(IO_3)_4$ is colorless, its transparency in the visible domain makes it a potential candidate for quadratic NLO applications and radio communications, in the special case of frequency duplication [60].

Finally, we also computed the components C_{ij} of the elastic tensor C of $LiAl(IO_3)_4$, as listed in Table 3. As expected for a monoclinic structure [52], 13 independent values C_{ij} exist for $LiAl(IO_3)_4$. In order to be a considered as mechanically stable, a crystal structure at ambient pressure must fulfill the Born criterion, one of whose equivalent formulations is that the eigenvalues of the elastic tensor must all be positive [61]. The eigenvalues of the C tensor are shown in Table 4, and they are positive, confirming the stability of the structure.

Table 3. Elastic tensor components Cij for $LiAl(IO_3)_4$, in GPa, as obtained after a full geometry optimization. The errors obtained via DFT are provided in brackets.

C_{11}	C_{12}	C_{13}	C_{15}	C_{22}	C_{23}	C_{25}	C_{33}	C_{35}	C_{44}	C_{46}	C_{55}	C_{66}
78(3)	13.4(6)	23.6(7)	−1(1)	35(1)	21(1)	−4(1)	96(3)	1.6(2)	30.8(5)	−2.1(2)	41.3(5)	21(2)

Table 4. Eigenvalues of the elasticity matrix C of $LiAl(IO_3)_4$, in GPa.

λ_1	λ_2	λ_3	λ_4	λ_5	λ_6
19.61	26.45	31.19	42.3	61.58	118.96

The computed elastic coefficients are of the same order of magnitude as other NLO materials [62]. Elastic properties such as the bulk (*B*), shear (*G*), and Young's (*E*) moduli in the Voigt, Reuss, and Hill approximations, and the corresponding Poisson ratio *P*, were calculated and are summarized in Table 5. The calculated bulk modulus *B* of $LiAl(IO_3)_4$ was found to be 28.7–36.1 GPa, indicating that $LiAl(IO_3)_4$ is a fairly compressible material. The obtained bulk modulus is comparable to that of $Co(IO_3)_2$ (*B* = 29.8 GPa) and $Zn(IO_3)_2$ (*B* = 21.6 GPa), which are structurally related to $LiAl(IO_3)_4$ [25,43]. On the other hand, the obtained Poisson ratio is in the lower limits of the typical value for solids [63], and *B/G* is 1.17–126, suggesting that $LiAl(IO_3)_4$ is a brittle material [63].

Table 5. Bulk (*B*), shear (*G*) and Young's (*E*) moduli, and the Poisson ratio for $LiAl(IO_3)_4$.

	Voigt	Reuss	Hill
B (GPa)	32.4	36.1	28.7
G (GPa)	26.5	28.6	24.4
E (GPa)	62.5	67.9	57.0
Poisson ratio	0.18	0.19	0.17

4. Conclusions

We have reported a novel experimental approach for a facile and cost-effective synthesis of likely nontoxic $LiAl(IO_3)_4$ nanocrystals, having potentially high IR NLO performances as exogenous optical biomarkers. The method makes use of a soft-chemistry technique, resulting within a few hours in precipitated nanoparticles from almost saturated solutions of the reagents. No hydrothermal processing is needed. The synthesized samples have been characterized by X-ray diffraction, scanning electron microscopy, EDX, UV-Vis, FTIR,

and Second Harmonic spectroscopy. According to XRD results and DFT calculations, the $P2_1$ monoclinic structure was assigned to $LiAl(IO_3)_4$, instead of to the $P6_3$ hexagonal space group as previously proposed. Additionally, we also determined an average nanocrystal size at about 23 nm from Le Bail refinements and Williamson-Hall plots. The chemical composition and the expected stoichiometry of the nanocrystals were confirmed by both XRD and EDX. The optical band gap of the nanoparticles was estimated to be 3.43(3) eV, using absorption spectroscopy.

DFT simulations supported our findings about the crystal structure of $LiAl(IO_3)_4$. Theoretical calculations of the band structure showed that $LiAl(IO_3)_4$ is an indirect semiconductor with a calculated band gap E_{gap} = 3.68 eV, close to the experimental value. Additionally, the theoretical study of the optical properties suggested that $LiAl(IO_3)_4$ has a birefringence index D = 0.21, close to that of the zinc iodate $Zn(IO_3)_2$.

Author Contributions: Conceptualization, Z.H.; formal analysis, R.C., Z.H., M.A.F., S.B., A.B., K.B., R.L.D. and J.C.M.; investigation, R.C. and Z.H.; supervision, Z.H.; validation, E.B., A.L., Y.M. and D.E.; visualization, E.B. and D.E.; writing—original draft, R.C. and Z.H.; writing—review and editing, R.C., Z.H., E.B., A.L., Y.M. and D.E. All authors have read and agreed to the published version of the manuscript.

Institutional Review Board Statement: Not applicable.

Informed Consent Statement: Not applicable.

Data Availability Statement: Data from experiments and calculations are available at request from the authors.

Conflicts of Interest: The authors declare no conflict of interest. The funders had no role in the design of the study, in the collection, analyses, or interpretation of data, in the writing of the manuscript, or in the decision to publish the results.

References

1. Tenne, R. Fullerene-like materials and nanotubes from inorganic compounds with a layered (2-D) structure. *Colloids Surfaces A Physicochem. Eng. Asp.* **2002**, *208*, 83–92. [CrossRef]
2. Huang, X.; Boey, F.; Zhang, H. A Brief Review on Graphene-Nanoparticle Composites. *Cosmos* **2010**, *06*, 159–166. [CrossRef]
3. Ramesh, S. Sol-Gel Synthesis and Characterization of $Ag_{3(2+x)}Al_xTi_{4-x}O_{11}+\delta$ ($0.0 \leq x \leq 1.0$) Nanoparticles. *J. Nanosci.* **2013**, *2013*, 1–8. [CrossRef]
4. Mann, S.; Burkett, S.L.; Davis, S.A.; Fowler, C.E.; Mendelson, N.H.; Sims, S.D.; Walsh, D.; Whilton, N.T. Sol–Gel Synthesis of Organized Matter. *Chem. Mater.* **1997**, *9*, 2300–2310. [CrossRef]
5. Tai, C.Y.; Tai, C.-T.; Chang, M.-H.; Liu, H.-S. Synthesis of Magnesium Hydroxide and Oxide Nanoparticles Using a Spinning Disk Reactor. *Ind. Eng. Chem. Res.* **2007**, *46*, 5536–5541. [CrossRef]
6. Bhaviripudi, S.; Mile, E.; Steiner, S.A.; Zare, A.T.; Dresselhaus, M.S.; Belcher, A.M.; Kong, J. CVD Synthesis of Single-Walled Carbon Nanotubes from Gold Nanoparticle Catalysts. *J. Am. Chem. Soc.* **2007**, *129*, 1516–1517. [CrossRef]
7. Kammler, H.K.; Mädler, L.; Pratsinis, S.E. Flame Synthesis of Nanoparticles. *Chem. Eng. Technol.* **2001**, *24*, 583–596. [CrossRef]
8. Kuppusamy, P.; Yusoff, M.M.; Maniam, G.P.; Govindan, N. Biosynthesis of metallic nanoparticles using plant derivatives and their new avenues in pharmacological applications—An updated report. *Saudi Pharm. J.* **2016**, *24*, 473–484. [CrossRef]
9. Prasad Yadav, T.; Manohar Yadav, R.; Pratap Singh, D. Mechanical Milling: A Top Down Approach for the Synthesis of Nanomaterials and Nanocomposites. *Nanosci. Nanotechnol.* **2012**, *2*, 22–48. [CrossRef]

10. Pimpin, A.; Srituravanich, W. Review on Micro- and Nanolithography Techniques and their Applications. *Eng. J.* **2012**, *16*, 37–56. [CrossRef]

11. Amendola, V.; Meneghetti, M. Laser ablation synthesis in solution and size manipulation of noble metal nanoparticles. *Phys. Chem. Chem. Phys.* **2009**, *11*, 3805. [CrossRef]

12. Shah, P.; Gavrin, A. Synthesis of nanoparticles using high-pressure sputtering for magnetic domain imaging. *J. Magn. Magn. Mater.* **2006**, *301*, 118–123. [CrossRef]

13. Odularu, A.T. Metal Nanoparticles: Thermal Decomposition, Biomedicinal Applications to Cancer Treatment, and Future Perspectives. *Bioinorg. Chem. Appl.* **2018**, *2018*, 1–6. [CrossRef]

14. Regny, S.; Riporto, J.; Mugnier, Y.; Le Dantec, R.; Kodjikian, S.; Pairis, S.; Gautier-Luneau, I.; Dantelle, G. Microwave Synthesis and Up-Conversion Properties of SHG-Active α-(La, Er)(IO$_3$)$_3$ Nanocrystals. *Inorg. Chem.* **2019**, *58*, 1647–1656. [CrossRef] [PubMed]

15. Campargue, G.; La Volpe, L.; Giardina, G.; Gaulier, G.; Lucarini, F.; Gautschi, I.; Le Dantec, R.; Staedler, D.; Diviani, D.; Mugnier, Y.; et al. Multiorder Nonlinear Mixing in Metal Oxide Nanoparticles. *Nano Lett.* **2020**, *20*, 8725–8732. [CrossRef]

16. Wang, X.; Yang, L.; Chen, Z.; Shin, D.M. Application of Nanotechnology in Cancer Therapy and Imaging. *CA. Cancer J. Clin.* **2008**, *58*, 97–110. [CrossRef]

17. Staedler, D.; Magouroux, T.; Hadji, R.; Joulaud, C.; Extermann, J.; Schwung, S.; Passemard, S.; Kasparian, C.; Clarke, G.; Gerrmann, M.; et al. Harmonic Nanocrystals for Biolabeling: A Survey of Optical Properties and Biocompatibility. *ACS Nano* **2012**, *6*, 2542–2549. [CrossRef] [PubMed]

18. Chi, E.O.; Ok, K.M.; Porter, Y.; Halasyamani, P.S. Na$_2$Te$_3$Mo$_3$O$_{16}$: A New Molybdenum Tellurite with Second-Harmonic Generating and Pyroelectric Properties. *Chem. Mater.* **2006**, *18*, 2070–2074. [CrossRef]

19. Liang, M.-L.; Hu, C.-L.; Kong, F.; Mao, J.-G. BiFSeO$_3$: An Excellent SHG Material Designed by Aliovalent Substitution. *J. Am. Chem. Soc.* **2016**, *138*, 9433–9436. [CrossRef]

20. Liang, F.; Kang, L.; Lin, Z.; Wu, Y. Mid-Infrared Nonlinear Optical Materials Based on Metal Chalcogenides: Structure–Property Relationship. *Cryst. Growth Des.* **2017**, *17*, 2254–2289. [CrossRef]

21. Chang, H.-Y.; Kim, S.-H.; Halasyamani, P.S.; Ok, K.M. Alignment of Lone Pairs in a New Polar Material: Synthesis, Characterization, and Functional Properties of Li$_2$Ti(IO$_3$)$_6$. *J. Am. Chem. Soc.* **2009**, *131*, 2426–2427. [CrossRef]

22. Hebboul, Z.; Ghozlane, A.; Turnbull, R.; Benghia, A.; Allaoui, S.; Liang, A.; Errandonea, D.; Touhami, A.; Rahmani, A.; Lefkaier, I.K. Simple New Method for the Preparation of La(IO$_3$)$_3$ Nanoparticles. *Nanomaterials* **2020**, *10*, 2400. [CrossRef] [PubMed]

23. Benghia, A.; Hebboul, Z.; Chikhaoui, R.; Lefkaier, I.K.; Chouireb, A.; Goumri-Said, S. Effect of iodic acid concentration in preparation of zinc iodate: Experimental characterization of Zn(IO$_3$)$_2$, and its physical properties from density functional theory. *Vacuum* **2020**, *181*, 109660. [CrossRef]

24. Phanon, D.; Mosset, A.; Gautier-Luneau, I. New materials for infrared non-linear optics. Syntheses, structural characterisations, second harmonic generation and optical transparency of M(IO$_3$)$_3$ metallic iodates. *J. Mater. Chem.* **2007**, *17*, 1123. [CrossRef]

25. Liang, A.; Popescu, C.; Manjon, F.J.; Rodriguez-Hernandez, P.; Muñoz, A.; Hebboul, Z.; Errandonea, D. Structural and Vibrational Study of Zn(IO$_3$)$_2$ Combining High-Pressure Experiments and Density-Functional Theory. *Phys. Rev. B* **2021**, *103*, 054102. [CrossRef]

26. Liang, A.; Turnbull, R.; Bandiello, E.; Yousef, I.; Popescu, C.; Hebboul, Z.; Errandonea, D. High-Pressure Spectroscopy Study of Zn(IO$_3$)$_2$ Using Far-Infrared Synchrotron Radiation. *Crystals* **2020**, *11*, 34. [CrossRef]

27. Phanon, D.; Gautier-Luneau, I. Promising Material for Infrared Nonlinear Optics: NaI$_3$O$_8$ Salt Containing an Octaoxotriiodate(V) Anion Formed from Condensation of [IO$_3$]$^-$ Ions. *Angew. Chemie Int. Ed.* **2007**, *46*, 8488–8491. [CrossRef]

28. Bonacina, L.; Mugnier, Y.; Courvoisier, F.; Le Dantec, R.; Extermann, J.; Lambert, Y.; Boutou, V.; Galez, C.; Wolf, J.-P. Polar Fe(IO$_3$)$_3$ nanocrystals as local probes for nonlinear microscopy. *Appl. Phys. B* **2007**, *87*, 399–403. [CrossRef]

29. Extermann, J.; Bonacina, L.; Cuña, E.; Kasparian, C.; Mugnier, Y.; Feurer, T.; Wolf, J.-P. Nanodoublers as deep imaging markers for multi-photon microscopy. *Opt. Express* **2009**, *17*, 15342. [CrossRef]

30. Jia, Y.; Chen, Y.; Guo, Y.; Guan, X.; Li, C.; Li, B.; Liu, M.; Zhang, X. LiM^{II}(IO$_3$)$_3$ (M^{II} =Zn and Cd): Two Promising Nonlinear Optical Crystals Derived from a Tunable Structure Model of α-LiIO$_3$. *Angew. Chem.* **2019**, *131*, 17354–17358. [CrossRef]

31. Hu, C.-L.; Mao, J.-G. Recent advances on second-order NLO materials based on metal iodates. *Coord. Chem. Rev.* **2015**, *288*, 1–17. [CrossRef]

32. Liang, A.; Rahman, S.; Rodriguez-Hernandez, P.; Muñoz, A.; Manjón, F.J.; Nenert, G.; Errandonea, D. High-Pressure Raman Study of Fe(IO$_3$)$_3$: Soft-Mode Behavior Driven by Coordination Changes of Iodine Atoms. *J. Phys. Chem. C* **2020**, *124*, 21329–21337. [CrossRef]

33. Peter, S.; Pracht, G.; Lange, N.; Lutz, H.D. Zinkiodate - Schwingungsspektren (IR, Raman) und Kristallstruktur von Zn(IO$_3$)$_2 \cdot 2H_2O$. *Zeitschrift für Anorg. und Allg. Chemie* **2000**, *626*, 208–215. [CrossRef]

34. Bentria, B.; Benbertal, D.; Bagieu-Beucher, M.; Mosset, A.; Zaccaro, J. Crystal engineering strategy for quadratic nonlinear optics. Part II: Hg(IO$_3$)$_2$. *Solid State Sci.* **2003**, *5*, 359–365. [CrossRef]

35. Liang, A.; Rahman, S.; Saqib, H.; Rodriguez-Hernandez, P.; Muñoz, A.; Nénert, G.; Yousef, I.; Popescu, C.; Errandonea, D. First-Order Isostructural Phase Transition Induced by High Pressure in Fe(IO$_3$)$_3$. *J. Phys. Chem. C* **2020**, *124*, 8669–8679. [CrossRef]

36. Taouti, M.B.; Suffren, Y.; Leynaud, O.; Benbertal, D.; Brenier, A.; Gautier-Luneau, I. Structures, Thermal Behaviors, and Luminescent Properties of Anhydrous Lanthanum Iodate Polymorphs. *Inorg. Chem.* **2015**, *54*, 3608–3618. [CrossRef] [PubMed]

37.   Hebboul, Z.; Galez, C.; Benbertal, D.; Beauquis, S.; Mugnier, Y.; Benmakhlouf, A.; Bouchenafa, M.; Errandonea, D. Synthesis, characterization, and crystal structure determination of a new lithium zinc iodate polymorph LiZn(IO$_3$)$_3$. *Crystals* **2019**, *9*, 464. [CrossRef]

38.   Ok, K.M.; Halasyamani, P.S. New Metal Iodates: Syntheses, Structures, and Characterizations of Noncentrosymmetric La(IO$_3$)$_3$ and NaYI$_4$O$_{12}$ and Centrosymmetric β-Cs$_2$I$_4$O$_{11}$ and Rb$_2$I$_6$O$_{15}$(OH)$_2$·H$_2$O. *Inorg. Chem.* **2005**, *44*, 9353–9359. [CrossRef]

39.   Clark, S.J.; Segall, M.D.; Pickard, C.J.; Hasnip, P.J.; Probert, M.I.J.; Refson, K.; Payne, M.C. First principles methods using CASTEP. *Zeitschrift für Krist.—Cryst. Mater.* **2005**, *220*, 567–570. [CrossRef]

40.   Perdew, J.P.; Burke, K.; Ernzerhof, M. Generalized gradient approximation made simple. *Phys. Rev. Lett.* **1996**, *77*, 3865–3868. [CrossRef]

41.   Heyd, J.; Scuseria, G.E.; Ernzerhof, M. Erratum: "Hybrid functionals based on a screened Coulomb potential" [J. Chem. Phys. 118, 8207 (2003)]. *J. Chem. Phys.* **2006**, *124*, 219906. [CrossRef]

42.   Lingfen, Z.; Chaoguo, W. The Study of LiAl(IO$_3$)$_4$ Crystal Structure. *J. Guangxi Univ. (Nat. Sci. Ed.)* **1993**, *18*, 81–83.

43.   Liang, A.; Popescu, C.; Manjon, F.J.; Turnbull, R.; Bandiello, E.; Rodriguez-Hernandez, P.; Muñoz, A.; Yousef, I.; Hebboul, Z.; Errandonea, D. Pressure-Driven Symmetry-Preserving Phase Transitions in Co(IO$_3$)$_2$. *J. Phys. Chem. C* **2021**, *125*, 17448–17461. [CrossRef]

44.   Balzar, D.; Ledbetter, H. Voigt-function modeling in Fourier analysis of size- and strain-broadened X-ray diffraction peaks. *J. Appl. Crystallogr.* **1993**, *26*, 97–103. [CrossRef]

45.   Warren, B.E.; Averbach, B.L. The Separation of Cold-Work Distortion and Particle Size Broadening in X-Ray Patterns. *J. Appl. Phys.* **1952**, *23*, 497. [CrossRef]

46.   Hall, W.H. X-Ray Line Broadening in Metals. *Proc. Phys. Soc. Sect. A* **1949**, *62*, 741–743. [CrossRef]

47.   Chen, X.; Xue, H.; Chang, X.; Zang, H.; Xiao, W. Hydrothermal synthesis and crystal structures of Nd(IO$_3$)$_3$ and Al(IO$_3$)$_3$. *J. Alloys Compd.* **2005**, *398*, 173–177. [CrossRef]

48.   Tauc, J. Optical properties and electronic structure of amorphous Ge and Si. *Mater. Res. Bull.* **1968**, *3*, 37–46. [CrossRef]

49.   Urbain, M.; Riporto, F.; Beauquis, S.; Monnier, V.; Marty, J.-C.; Galez, C.; Durand, C.; Chevolot, Y.; Dantec, R.L.; Mugnier, Y. On the Reaction Pathways and Growth Mechanisms of LiNbO$_3$ Nanocrystals from the Non-Aqueous Solvothermal Alkoxide Route. *Nanomaterials* **2021**, *11*, 154. [CrossRef]

50.   Riporto, J.; Urbain, M.; Mugnier, Y.; Multian, V.; Riporto, F.; Bredillet, K.; Beauquis, S.; Galez, C.; Monnier, V.; Chevolot, Y.; et al. Second harmonic spectroscopy of ZnO, BiFeO$_3$ and LiNbO$_3$ nanocrystals. *Opt. Mater. Express* **2019**, *9*, 1955. [CrossRef]

51.   Feynman, R.P. Forces in Molecules. *Phys. Rev.* **1939**, *56*, 340–343. [CrossRef]

52.   Nye, J.F. *Physical Properties of Crystals. Their Representation by Tensors and Matrices*; Oxford University Press: Oxford, UK, 1985.

53.   Song, H.; Jiang, D.; Wang, N.; Xing, W.; Guo, R.; Lin, Z.; Yao, J.; Wang, Y.; Tu, H.; Zhang, G. Na$_3$Bi(IO$_3$)$_6$: An Alkali-Metal Bismuth Iodate with Intriguing One-Dimensional [BiI$_6$O$_{18}$] Chains and Pressure-Induced Structural Transition. *Inorg. Chem.* **2021**, *60*, 2893–2898. [CrossRef]

54.   Chen, J.; Hu, C.-L.; Mao, F.-F.; Zhang, X.-H.; Yang, B.-P.; Mao, J.-G. LiMg(IO$_3$)$_3$: An excellent SHG material designed by single-site aliovalent substitution. *Chem. Sci.* **2019**, *10*, 10870–10875. [CrossRef]

55.   Xiao, L.; Cao, Z.; Yao, J.; Lin, Z.; Hu, Z. A new cerium iodate infrared nonlinear optical material with a large second-harmonic generation response. *J. Mater. Chem. C* **2017**, *5*, 2130–2134. [CrossRef]

56.   Luo, M.; Liang, F.; Hao, X.; Lin, D.; Li, B.; Lin, Z.; Ye, N. Rational Design of the Nonlinear Optical Response in a Tin Iodate Fluoride Sn(IO$_3$)$_2$F$_2$. *Chem. Mater.* **2020**, *32*, 2615–2620. [CrossRef]

57.   Liang, A.; Rodriguez-Hernandez, P.; Muñoz, A.; Rahman, S.; Segura, A.; Errandonea, D. Pressure-dependent modifications in the optical and electronic properties of Fe(IO$_3$)$_3$: The role of Fe 3d and I 5p lone–pair electrons. *Inorg. Chem. Front.* **2021**. [CrossRef]

58.   Dahame, T.; Fadla, M.A.; Bentria, B.; Benghia, A. Electronic, elastic, linear and nonlinear optical properties of beryllium based chalcopyrite BeMN$_2$ (M = C, Si): An ab-initio study. *Phys. B Condens. Matter* **2019**, *561*, 37–42. [CrossRef]

59.   Temzini, R.; Fadla, M.A.; Dahame, T.; Bentria, B. Natural and induced birefringence using electro optic effect; ZnS and CuAlS$_2$ crystals. *Optik (Stuttg)* **2020**, *217*, 164917. [CrossRef]

60.   Hebboul, Z. Cadmium Iodate Syntheses and Characterization. In *Heavy Metals*; InTechOpen: London, UK, 2018.

61.   Mouhat, F.; Coudert, F.X. Necessary and sufficient elastic stability conditions in various crystal systems. *Phys. Rev. B—Condens. Matter Mater. Phys.* **2014**, *90*, 4–7. [CrossRef]

62.   Kanoun, M.B.; Goumri-Said, S. Effect of alloying on elastic properties of ZrN based transition metal nitride alloys. *Surf. Coatings Technol.* **2014**, *255*, 140–145. [CrossRef]

63.   Errandonea, D.; Ferrer-Roca, C.; Martínez-Garcia, D.; Segura, A.; Gomis, O.; Muñoz, A.; Rodríguez-Hernández, P.; López-Solano, J.; Alconchel, S.; Sapiña, F. High-pressure x-ray diffraction and ab initio study of Ni$_2$Mo$_3$N, Pd$_2$Mo$_3$N, Pt$_2$Mo$_3$N, Co$_3$Mo$_3$N, and Fe$_3$Mo$_3$N: Two families of ultra-incompressible bimetallic interstitial nitrides. *Phys. Rev. B* **2010**, *82*, 174105. [CrossRef]